Available online at www.sciencedirect.com
ScienceDirect
Journal of Nuclear Materials 361 (2007) 149–159
journal of nuclear materials
www.elsevier.com/locate/jnucmat

Kinetics of coarsening of helium bubbles during implantation and post-implantation annealing

S.I. Golubov [a,b], R.E. Stoller [a,*], S.J. Zinkle [a], A.M. Ovcharenko [c]

[a] *Materials Science and Technology Division, Oak Ridge National Laboratory, P.O. Box 2008, Oak Ridge, TN 37831-6138, USA*
[b] *Center for Materials Processing, The University of Tennessee, East Stadium Hall, Knoxville, TN 37996-0750, USA*
[c] *ARIAM, 82 Lenin Av., Obninsk, Kaluga Region 249038, Russian Federation*

Abstract

To understand the effects of He on irradiated metals requires modeling of helium-vacancy cluster evolution. A new method of solving the two-dimensional master equation (ME) describing He-vacancy cluster evolution has been applied to calculate helium bubble evolution in a stainless steel irradiated with alpha particles near room temperature and annealed in the temperature range of 600–900 °C. For the first time, the evolution of the helium bubble size distribution function was precisely calculated in 2-D phase space and good agreement with experimental results was obtained. The results indicate that Brownian motion of bubbles via surface vacancy diffusion provides a reasonable explanation for bubble evolution during annealing, most bubbles are found to be near the equilibrium state during the evolution at temperatures of 700 °C and higher, lack of vacancies at temperatures lower than 700 °C prevents bubble growth, and use of a non-ideal He equation of state (EOS) increases the bubble density and size relative to the case when the ideal EOS is used.

PACS: 61.80.Az; 61.72.Cc; 61.72.Ji; 61.72.Qq

---

1. Introduction

Precipitation of helium introduced into metals by (n, α) reactions that occur in fission and fusion reactors influences microstructure evolution of materials. It has been established that helium atoms assist the nucleation and growth of cavities in irradiated materials leading to swelling and mechanical property changes. Modeling of helium-vacancy cluster evolution is required to develop an understanding of the role of He. The literature contains several partial treatments of the problem where two coarsening mechanisms, namely Ostwald ripening (OR) [1–13] and bubble migration and coalescence (BMC) [14–20,7,21–25] have been considered. However an accurate treatment of the second mechanism is complicated and the previous work has been done in a semi-quantitative way. For example, when, calculating bubble coalescence driven by BMC, it has commonly been assumed that bubbles maintain mechanical equilibrium during their evolution. Such an approach simplifies the calculations by permitting the transformation of a 2-D kinetic equation describing the evolution two independent variables

---

[*] Corresponding author.
E-mail address: rkn@ornl.gov (R.E. Stoller).

0022-3115/$ - see front matter © 2006 Elsevier B.V. All rights reserved.
doi:10.1016/j.jnucmat.2006.12.032

(numbers of He atoms and vacancies) into a 1-D in which this number of vacancies is determined by the number of He atoms in accordance with a certain EOS. However the validity of the assumption has not been proven. The present work addresses this problem.

In the framework of a mean field approach, the most general description of cluster evolution is based on the so-called master equation (ME), which summarizes a large number of differential (or integral–differential when BMC is taken into account) equations. In order to be realistic, it is necessary to consider clusters containing a large number of point defects/atoms, thus the number of equations is normally too large to be used in numerical calculations. However the ME can be solved by means of numerical methods using procedures, which allow reducing the number of equations significantly. The grouping method first developed by Kiritani [26] for describing the evolution of vacancy loops during ageing of quenched metals was intended to provide such a procedure. However, it was shown in [27] the method is not accurate because the grouping equations are not faithful to the original ME. The problem arises due to the main assumption made in [26] that a group of equations can be replaced with a single 'averaged' equation. A similar problem arises for any grouping method using the same assumption. Note that the calculation of cluster evolution driven by both coarsening mechanisms has not been subjected to any specific grouping method of the type mentioned.

It has been shown [27] that for the case of 1-D ME when cluster evolution is driven by OR only, the simplest accurate grouping method may be obtained when the size distribution function (SDF) within a group is approximated by a linear function. Such an approximation maintains the identity of the grouped ME with the original, while satisfying the conservation laws for both the total number of clusters and the total number of point defects accumulated in the clusters. In [28] the grouping method was generalized to the case of 2-D ME. Moreover, it appears that the grouping method can be also generalized to take into account bubble migration and coalescence [29]. Thus, in the framework of the generalized grouping method describing evolution of the clusters equal accuracy can be obtained for the general case when the evolution is driven simultaneously by cluster interactions with mobile point defects, and by Brownian motion of the clusters.

The present study focuses on application of the grouping method to model He-vacancy cluster evolution in a stainless steel irradiated with alpha particles near room temperature and annealed in the temperature range of 600–900 °C [30]. The ME used and a short description of the grouping method are provided in Section 2. Experimental data on He-vacancy cluster evolution in a stainless steel [30] and set of material and irradiation parameters used in the calculations are given in Section 3. Results of the calculations are presented in Section 4.

2. Outline of modeling

To describe the evolution of He-vacancy clusters driven by reactions with mobile point defects and Brownian motion and coalescence of the clusters, the following ME has to be solved in a two-dimensional phase space of x, m (x and m are the number vacancies and He atoms, respectively)

$$\begin{aligned}\frac{\mathrm{d}f(x,m)}{\mathrm{d}t} &= -(\nabla_x J_x(x,m,t) + \nabla_m J_m(x,m,t)) \\ &\quad - f(x,m)\sum_{\substack{x'\geqslant 1,x'\neq x\\ m'\geqslant 0,m'\neq m}} \Lambda_{xm,x'm'} f(x',m') \\ &\quad - 2f^2(x,m)\Lambda_{xm,xm} + \sum_{\substack{x'\leqslant x-2\\ m'\leqslant m}} \Lambda_{x'm',x-x',m-m'} \\ &\quad \times f(x',m')f(x-x',m-m'), \qquad (1)\end{aligned}$$

where the first term describes cluster evolution driven by cluster interaction with point defects (∇_x, ∇_m are divergences in x and m space, correspondently) and other terms describe the impact of cluster Brownian motion and coalescence. In Eq. (1) $f(x,m,t)$ and $J_x\ (x,m,t)$, $J_m\ (x,m,t)$ are the size distribution function (SDF) and fluxes of clusters in x and m-spaces, respectively; and $\Lambda_{x'm',x''m''}$ is the collision cross section between the clusters containing x', m' and x'', m'' vacancies and He atoms, respectively. The fluxes are determined by the reactions of clusters with point defects and may be presented as follows:

$$\begin{aligned}J_x(x,m,t) &= P_x(x,m,t)f(x,m,t) \\ &\quad - Q_x(x+1,m,t)f(x+1,m,t), \\ J_m(x,m,t) &= P_m(x,m,t)f(x,m,t) \\ &\quad - Q_m(x,m+1,t)f(x,m+1,t),\end{aligned} \qquad (2)$$

where the coefficients $P_x(x,t)$, $Q_x(x,m,\ t)$,$P_m(x,t)$, and $Q_m\ (x,m,t)$ are the cluster reaction rates for capture (P) and evaporation (Q) of mobile point defects (vacancies, SIAs and He atoms) leading to a change in the cluster of sizes x and m, respectively; $\Lambda_{x'm',x''m''}$ is the cross-section for randomly migrating spherical particles. $\Lambda_{x'm',x''m''}$ was first derived by Chandrasekhar [31] and may be written in the following form:

$$\Lambda_{x'm',x''m''} = (48\pi^2/\Omega^2)^{1/3}[(x')^{1/3} + (x'')^{1/3}][D_{x'm'} + D_{x''m''}], \tag{3}$$

where Ω is the atomic volume and D_{xm} is diffusion coefficient of xm-cluster.

A ME in the form of Eq. (1) is a set of rate equations for the density of clusters of different sizes in the range of practical interest. As mentioned above, it is necessary to consider clusters containing such a large number of vacancies and He atoms that the numerical solution of Eq. (1) becomes practically impossible. The grouping method developed in [28,29] permits the number of equations to be reduced substantially, thus providing a tool which can be used for numerical calculations. The main idea of the grouping method [28] is that the xm phase space is divided into a series of groups with widths $\Delta x_i = x_i - x_{i-1}$, $\Delta m_j = m_j - m_{j-1}$, which include the clusters of the sizes $x_i = x_{i-1} + k$ $(k = 1, 2, \ldots, \Delta x_i)$, $m_j = m_{j-1} + n$ $(n = 1, 2, \ldots, \Delta m_j)$ and the SDF is approximated by a linear function within a group as follows:

$$f_{i,j}(x, m) = L_0^{i,j} + L_{1x}^{i,j}(x - \langle x\rangle_i) + L_{1m}^{i,j}(m - \langle m\rangle_j), \tag{4}$$

where $\langle x\rangle_i$, $\langle m\rangle_j$ are mean cluster sizes within the ij group. In Eq. (4) the subscript i indicates the number of a group in x-space and the subscript j indicates the number of a group in m-space. Thus within the grouping method one needs to calculate three coefficients $L_0^{i,j}$, $L_{1x}^{i,j}$, $L_{1m}^{i,j}$ for each group instead of number of equations equal to $n_{i,j} = \Delta x_i \Delta m_j$ required by Eq. (1).

It has been shown [28,29] that the simplest accurate form of the equations for the coefficients $L_0^{i,j}, L_{1x}^{i,j}, L_{1m}^{i,j}$ can be derived assuming that (a) the reaction rates with mobile defects for all cluster sizes within a group are equal, (b) rates of cluster coalescence for all clusters within a group are equal, and (c) coalescence of any two clusters belonging to the same or different groups, e.g. pq and $p'q'$, results in a cluster of bigger size belonging to a single group, e.g. ij, which satisfies the following conditions:

$$\begin{aligned} &x_{i-1} < (\langle x\rangle_p + \langle x\rangle_{p'}) \leqslant x_i, \\ &m_{j-1} < (\langle m\rangle_q + \langle m\rangle_{q'}) \leqslant m_j. \end{aligned} \tag{5}$$

In this case, equations for the coefficients $L_0^{i,j}, L_{1x}^{i,j}, L_{1m}^{i,j}$ are given by

$$\begin{aligned} \frac{\mathrm{d}L_0^{i,j}}{\mathrm{d}t} = {} & \frac{1}{\Delta x_i}[J_x(x_{i-1}, \langle m\rangle_j) - J_x(x_i, \langle m\rangle_j)] \\ & + \frac{1}{\Delta m_j}[J_m(\langle x\rangle_i, m_{j-1}) - J_m(\langle x\rangle_i, m_j)] \\ & - L_0^{i,j}(t)\left[\Lambda_{ij,ij}L_0^{i,j}(t)\Delta x_i \Delta m_j + \sum_{p,q}\Lambda_{ij,pq}L_0^{p,q}(t)\Delta x_p \Delta m_q\right] \\ & + \frac{1}{(\Delta x_i \Delta m_j)}\sum_{p,q}\sum_{p'q'}\Lambda_{pq,p'q'}L_0^{p,q}(t)L_0^{p',q'}(t)\Delta x_p \Delta m_q \Delta x_{p'} \Delta m_{q'}, \end{aligned} \tag{6}$$

$$\begin{aligned} \frac{\mathrm{d}L_{1x}^{i,j}}{\mathrm{d}t} = {} & -\left(\frac{\Delta x_i - 1}{2\sigma_i^2 \Delta x_i}\right)\Big\{J_x(x_{i-1}, \langle m\rangle_j) + J_x(x_i, \langle m\rangle_j) \\ & -2J_x\left(\langle x_i\rangle - \frac{1}{2}, \langle m\rangle_j\right)\Big\} \\ & + \frac{1}{\Delta m_j}\Big\{[J_m(\langle x\rangle_i + 1, m_{j-1}) - J_m(\langle x\rangle_i, m_{j-1})] \\ & - [J_m(\langle x\rangle_i + 1, m_j) - J_m(\langle x\rangle_i, m_j)]\Big\} \\ & + \sum_{p,q}\sum_{p',q'}\frac{\Delta x_p \Delta m_q \Delta x_{p'} \Delta m_{q'}}{(\Delta x_i \Delta m_j)\sigma_i^2}\Lambda_{pq,p'q'}L_0^{p,q}(t)L_0^{p',q'}(t) \\ & \times \left(\langle x\rangle_p + \langle x\rangle_{p'} - \langle x\rangle_i\right), \end{aligned} \tag{7}$$

$$\begin{aligned} \frac{\mathrm{d}L_{1m}^{i,j}}{\mathrm{d}t} = {} & -\left(\frac{\Delta m_j - 1}{2\sigma_j^2 \Delta m_j}\right)\Big\{J_m(\langle x\rangle_i, m_{j-1}) + J_m(\langle x\rangle_i, m_j) \\ & -2J_m\left(\langle x\rangle_i, \langle m\rangle_j - \frac{1}{2}\right)\Big\} \\ & + \frac{1}{\Delta x_i}\{[J_x(x_{i-1}, \langle m\rangle_j + 1) - J_x(x_{i-1}, \langle m\rangle_j)] \\ & - [J_x(x_i, \langle m\rangle_j + 1) - J_x(x_i, \langle m\rangle_j)]\} \\ & + \sum_{p,q}\sum_{p'q'}\frac{\Delta x_p \Delta m_q \Delta x_{p'} \Delta m_{q'}}{(\Delta x_i \Delta m_j)\sigma_j^2}\Lambda_{pq,p'q'}L_0^{p,q}(t)L_0^{p',q'}(t) \\ & \times \left(\langle m\rangle_q + \langle m\rangle_{q'} - \langle m\rangle_j\right) \end{aligned} \tag{8}$$

where

$$\begin{aligned} \sigma_i^2 &= \frac{1}{\Delta x_i}\left[\sum_{\lambda=x_{i-1}+1}^{x_i}\lambda^2 - \frac{1}{\Delta x_i}\left(\sum_{\lambda=x_{i-1}+1}^{x_i}\lambda\right)^2\right], \\ \sigma_j^2 &= \frac{1}{\Delta m_i}\left[\sum_{\lambda=m_{i-1}+1}^{m_i}\lambda^2 - \frac{1}{\Delta m_i}\left(\sum_{\alpha=m_{i-1}+1}^{m_i}\lambda\right)^2\right]. \end{aligned} \tag{9}$$

Eq. (9) gives dispersions of cluster sizes in the ij group. Note that summation in the last terms of Eq. (6)–(8) takes place over the groups pq and $p'q'$ satisfying Eq. (5). Note also that in the case when the group widths are taken to be equal to 1, i.e. $\Delta x_i = \Delta m_j = 1$, Eq. (6) is transformed to Eq. (1) $\left(L_0^{ij} \equiv f(x, m), \langle x\rangle_i \equiv x_i, \langle m\rangle_j \equiv m_j\right)$ whereas the right hand sides of Eqs. (7) and (8) turn out to be equal to zero, i.e. $L_{1,x}^{ij} = L_{1,m}^{ij} = 0$. In other words, there are no boundary problems between small size clusters, which are normally described by Eq. (1) $(\Delta x_i = \Delta m_j = 1)$ and the bigger ones when $\Delta x_i > 1$, $\Delta m_j > 1$.

Eqs. (6)–(8) represent ME within the grouping method and may be used to describe cluster evolution during irradiation or ageing. As can be seen from Eqs. (6)–(8), the basic values which determine the cluster evolution are the fluxes $J_x(x,m,t)$, $J_m(x,m,t)$ in the x, m size space and the cross-section $\Lambda_{x'x'',m'm''}$ for cluster coalescence. Here we will take into account mobility of vacancies, self interstitial atoms (SIAs) and He atoms in an interstitial configuration. The fluxes and corresponding rate equations for the mobile defects are given in [28]. The diffusion coefficient for clusters containing two or more vacancies is taken according to surface diffusion kinetics (see e.g. [32]).

$$D_{x_i,m_j} = D_{\langle x\rangle_i} = \frac{3}{2\pi} D_{\mathrm{S}} \left(\frac{\Omega^{1/3}}{\langle r\rangle_i} \right)^4, \tag{10}$$

where $D_{\mathrm{S}} = D_{\mathrm{S}}^0 \exp(-E_{\mathrm{S}}/kT)$ is the surface diffusion coefficient, Ω is atomic volume and $\langle r\rangle_i = (3\Omega\langle x\rangle_i/4\pi)^{1/3}$ is the mean radius of the ij group of clusters. In our calculations it is assumed that the smallest clusters ($x = 1$) are immobile and can contain up to 4 helium atoms. The gas pressure in the clusters, which determines cluster stability, is computed using a non-ideal equation of He state derived by Manzke and Trinkaus [33,34].

The set of Eqs. (6)–(8) together with the equations for the mobile defects has been numerically integrated using the so-called Modified Euler method [35]. The calculations have been performed for the cases:

1. Helium pre-implantation regime, when He-vacancy cluster evolution takes place under the concurrent processes of Frenkel pair production and He implantation, and
2. Thermal annealing regime, when bubble evolution takes place via Brownian motion and coalescence of bubbles and their reactions with thermally generated vacancies.

The initial conditions for the mobile defects and initial and boundary conditions for the SDF for step 1 are taken in the following form:

$$\begin{aligned} &C_v(t)_{|t=0} = C_{v0}, \\ &C_i(t=0)_{|t=0} = C_{\mathrm{He}}(t)_{|t=0} = 0, \\ &f(x,m,t)_{|t=0} = C_{v0}\delta(x-1)\delta(m), \quad (x \geqslant 1), \\ &f(x=1,0,t) = C_v(t), \quad f(x=\infty,m,t) = 0. \end{aligned} \tag{11}$$

In Eq. (11) $\delta(x)$ is the Kronneker delta. The initial and boundary conditions for the second step are taken from what was calculated during the first step.

3. Experimental data and parameters used in the calculations

In [30], specimens of model austenitic alloy P7 (Fe–17Cr–16.7Ni–2.5Mo) were implanted with about 40 appm He at room temperature and subsequently annealed for 1 h at temperatures between 600 and 900 °C. The temperature during implantation was less than 200 °C and the He implantation level in specimens used for the annealing varied between 32 and 47 appm. Helium bubble data measured after 1 h annealing are summarized in Table 1.

As can be seen from Table 1, He bubbles were found after 1 h annealing at all temperatures except 600 °C. In the temperature range of 700–900 °C the average size of bubbles increases and density decreases with increasing annealing temperature. Deviation from this behaviour observed at 800 °C (see Table 1) is probably a result of the higher level of implanted helium in the specimen used for annealing at 800 °C (see helium content calculated at the temperatures in Table 1 in [30]).

The calculations in the present work have been done by numerical integration of Eqs. (6)–(8) and corresponding rate equations for the mobile defects, i.e. for vacancies, self-interstitial atoms (SIAs) and He atoms in interstitial configuration. It is assumed

Table 1
Summary of bubble microstructures observed after 40 appm helium implantation in solution-annealed P7 and subsequent annealing for 1 h

Helium implanted (appm)	T (°C)	Density (10^{21} m^{-3})	Average radius (nm)	He content calculated (appm)
32	600	–	–	
44	700	8.25	0.82	15–17
37	750	6.33	1.09	25–29
47	800	6.66	1.57	69–83
41	900	2.15	1.99	35–44

Table 2
He implantation parameters and material parameters used in the calculations

Helium generation rate	2.0×10^{-3} appm/s
Implantation temperature	100 °C
Displacement rate during implantation	5.0×10^{-7} dpa/s
Implantation time	2.0×10^{4} s
Displacement dose	1.0×10^{-2} dpa
Helium implantation level	40 appm
Recombination coefficients	$5.0\times10^{+20}$ m^{-2}
Atomic volume, Ω	1.1777×10^{-29} m^{-3}
Vacancy diffusion coefficient pre-exponentional factor	8.0×10^{-05} m^{2}/s
Migration energy	1.40 eV
SIA diffusion coefficient, pre-exponentional factor	8.0×10^{-08} m^{2}/s
Migration energy	0.15 eV
He atom diffusion coefficient pre-exponentional factor	8.0×10^{-08} m^{2}/s
Migration energy	0.15 eV
Dislocation density	10^{13} m^{-2}
Surface energy	$(3.24-1.4\times T$ (°C)/1000) J/m^{2} [37]
Dislocation capture efficiency for vacancies	1.00
Dislocation capture efficiency for SIAs	1.25
Surface diffusion coefficient, D_S pre-exponentional factor	4.65×10^{-9} m^{2}/s
Migration energy	1.40 eV

that the implantation temperature was equal to 100 °C and all specimens were implanted with He to a level of 40 appm. The implantation parameters and material parameters used in our calculations are summarized in Table 2.

4. Results

4.1. He accumulation during implantation

The calculations are carried out to a dose of 10^{-2} dpa when the total He concentration reached a level of 40 appm. It is found vacancy concentration under irradiation does not reach steady state level because of their low mobility. Under this condition He atoms are mainly accumulated in clusters of the smallest size, $x=1$, since the total flux of SIAs to He-V clusters remains larger than that of vacancies. Thus the terminal SDF after irradiation is found to be close to a delta function in x-space whereas in m-space it covers an area from $m=0$ to $m=4$. This calculated SDF is used as input to the subsequent calculations of bubble evolution during the annealing at temperatures in a range of 600–900 °C.

4.2. Bubble evolution during annealing

As mentioned above, the smallest He-vacancy clusters, i.e. cluster of size $x=1$, are considered to be immobile. Since thermal resolution of He atoms from the clusters is not taken into account in our calculations, the onset of bubble evolution takes place via reactions between freely migrating vacancies and the smallest clusters. Indeed, such reactions lead to the formation of the clusters of di-vacancy type, which migrate via the surface diffusion mechanism (see Eq. (10)). As a result, the clusters of bigger sizes, i.e. clusters with $x>2$, may be formed via interaction between the di-vacancy clusters and the smallest clusters of $x=1$ providing a mechanism He transport from small clusters to the bigger ones, i.e. bubble evolution. The activation energy for surface diffusion, E_S, and the pre-exponentional factor, D_S^0, were used as fitting parameters in the calculations. It was found that the results obtained for the case when E_S is taken to be equal to the volume vacancy migration energy and $D_S^0=4.65\times10^{-9}$ m^2/s agrees quite well with the observations. More detailed characterization of the results calculated is presented below.

4.2.1. Annealing in the temperature range of 700–900 °C

The calculations have been carried for all annealing temperatures used in [30]. It was found that the 2-D bubble size distribution functions, $f(x,m)$, calculated in this temperature range exhibit quite similar behaviour. Namely, bubbles were found to be distributed in wide range of x, m-space but are mainly concentrated along certain trajectories which correspond to equilibrium bubbles, i.e. those bubbles which satisfied the equilibrium equation $2\gamma/r(x) = p(x,m,T)$, where $p(x,m,T)$ is gas pressure, $r(x)$ is bubble radius, T is absolute temperature and γ is the surface energy. Moreover, such a SDF is maintained throughout annealing time. An example can be seen in Figs. 1(a) and 1(b) where 2-D size distribution functions calculated at 800 °C for annealing times of 380 s and 1 h are presented. The plots show that the SDF was indeed located along the equilibrium trajectory shown in the plots by the red solid lines. The same trend in bubble evolution is found to take place at other temperatures as illustrated in Figs. 2(a) and 2(b) where the terminal SDFs calculated for the case of 1 h annealing at the temperatures of 700 and 900 °C are presented. Thus, one can conclude that the assumption that bubbles are maintained in mechanical equilibrium during annealing used in earlier models is quite realistic. Note that the scale of the density axis in Figs. 1(a), 2(a) and 1(b), 2(b) is different whereas the scale of x,m-space is the same in all plots.

A comparison of the calculation results with those measured is given in Figs. 3(a), 3(b) and 4(a), 4(b). In Figs. 3(a), 3(b) integral parameters such as number density and average size of bubbles calculated at different temperatures for the case of implantation of 40 appm He are presented together with the measured results [30]. The calculated results agree well with the observations. To illustrate sensitivity of the calculated bubble density and size to the He content, calculated results obtained for the case of implantations of 20 appm at 700 °C and 80 appm at 800 °C (see last column in Table 1) are also presented in the plots. Variations in He content change are calculated in such a way to improve their agreement with the experimental values [30].

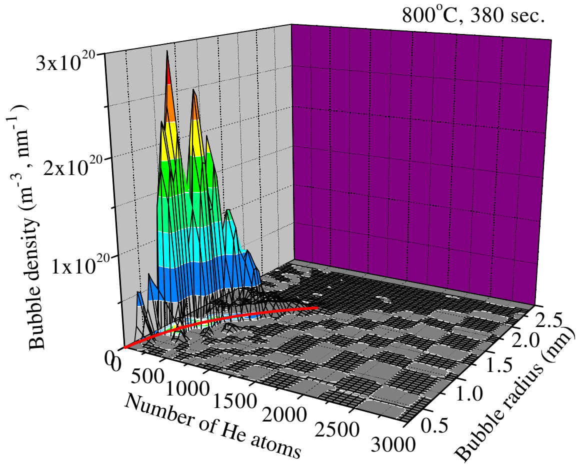

Fig. 1(a). Bubble size distribution calculated at 800 °C after annealing for 380 s.

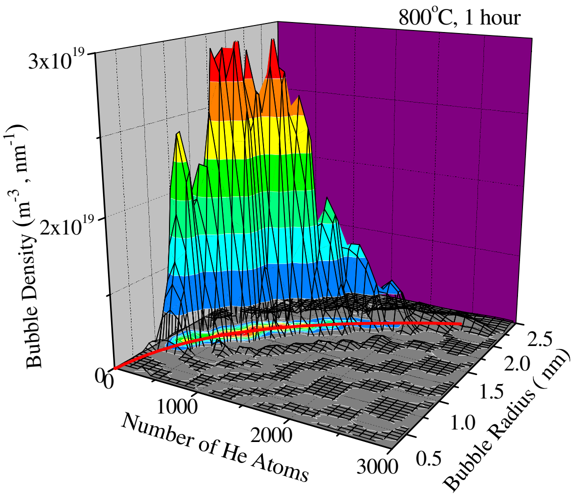

Fig. 1(b). Bubble size distribution calculated at 800 °C after annealing for 1 h. Note that the scale of the density axis is 10 times smaller than that in 1(a).

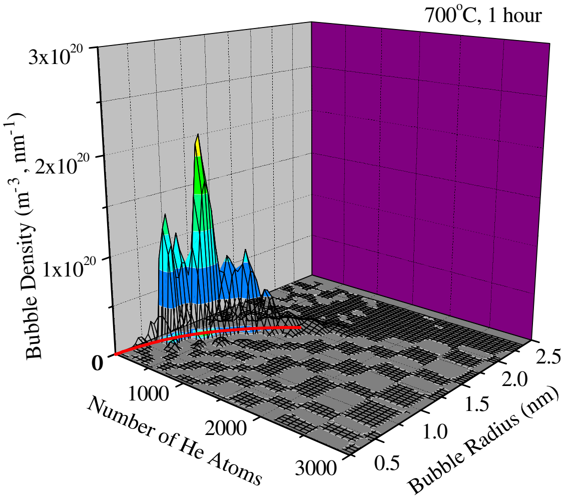

Fig. 2(a). Bubble size distribution calculated at 700 °C after annealing for 1 h.

Calculated and measured [30] 1-D size distribution functions ($f(x) = \sum_m f(x,m)$) for different temperatures are presented in Figs. 4(a) and 4(b). The measured and calculated SDFs are very close to each other at low temperatures 700 and 750 °C, whereas at higher temperatures the measured distributions are slightly wider than that the calculated

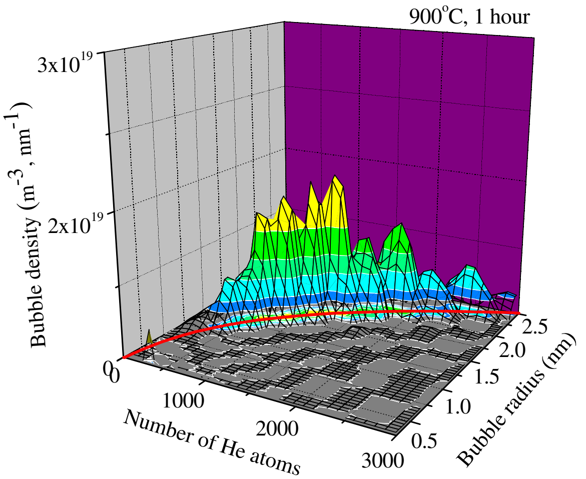

Fig. 2(b). Bubble size distribution calculated at 900 °C after annealing for 1 h. Note that the scale of the density axis is 10 times smaller comparing to that in 2(a).

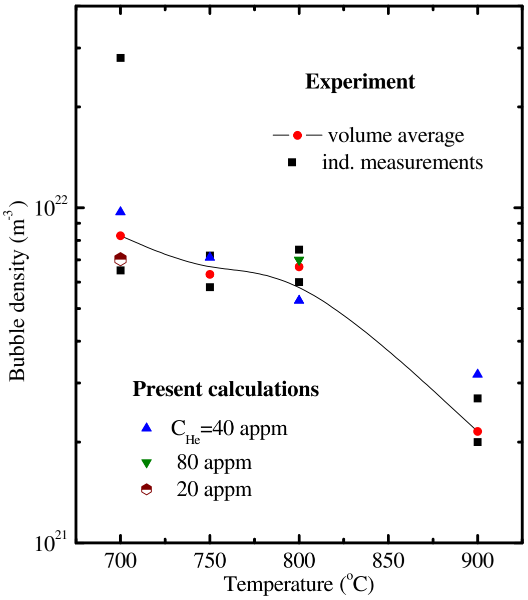

Fig. 3(a). Temperature dependence of the bubble number density calculated in the temperature range of 700–900 °C after annealing for 1 h. Observed bubble number density at the same temperatures is also presented.

ones. However the effect is rather small. Thus, one may conclude that the calculated results agree reasonably well with the observations. Note that thermal resolution of He atoms from bubbles, which is not taken into account in our calculations, is probably responsible for the width of the SDFs at higher temperatures.

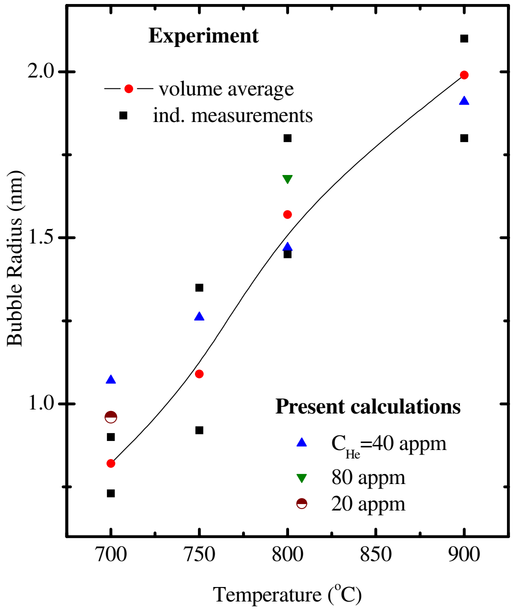

Fig. 3(b). Time dependence of the bubble size calculated in the temperature range of 700–900 °C after annealing for 1 h. Observed bubble size at the same temperatures is also presented.

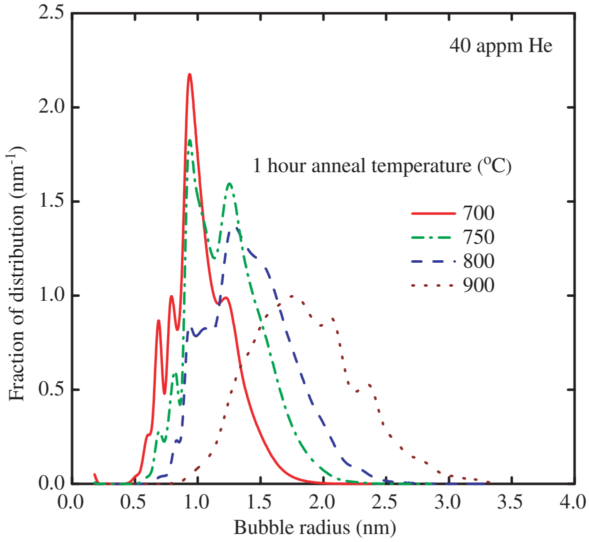

Fig. 4(a). One-dimensional bubble size distribution functions, i.e. $F(x) = \sum_m f(x,m)$, in the temperature range of 700–900 °C calculated after annealing for 1 h.

Note that the structure observed in the size distribution functions in Figs. 1, 2 and 4 is a result of including the mechanism of Brownian motion and coalescence. The size distribution functions normally have a smooth profile when evolution is controlled by emission and absorption of single defects

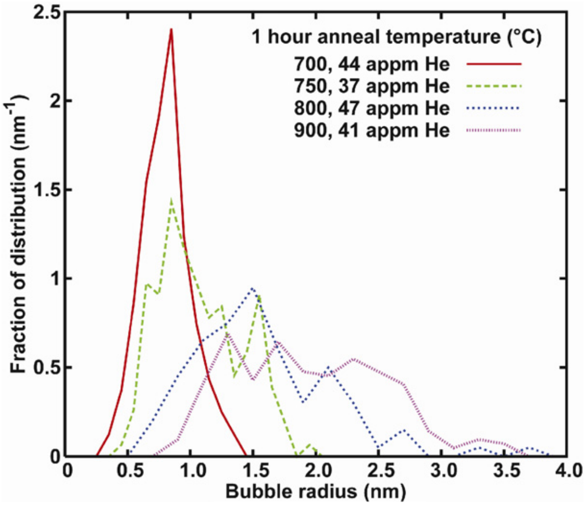

Fig. 4(b). Observed bubble size distributions at the same temperatures.

which leads to very small relative changes in the bubble size. For example, such a smooth SDF is observed when the current approach is used to simulate Ostwald ripening. In the case of BMC the change in cluster size due to coalescence is qualitatively different – a collision of two bubbles may lead to formation of a cluster with a size much larger than that of either bubble. Some support for this argument may be obtained from Fig. 4(b), where the experimentally measured SDF is presented.

4.2.2. Annealing at 600 °C

It was found that bubble evolution at this temperature is qualitatively different from that at 700 °C and higher temperatures. The calculations show that bubble evolution in this case is very limited and results in formation of bubbles with a mean size of about 1 nm in diameter during 1 h annealing. This is close to the size limit of bubbles to be detected by TEM. Close examination shows that the decrease in bubble growth is caused not only by a decrease in their mobility but also because of the lack of vacancies available to contribute the evolution since the annealing time of 1 h is not enough to reach the thermal equilibrium vacancy concentration. As a result, bubbles at this temperature are over-pressurized with respect to the equilibrium value of gas pressure caused by surface tension ($2\gamma/r(x)$) as can be seen in Fig. 5. Correspondingly their size increases with time as about $\langle r\rangle \propto t^{1/8}$ instead of $\langle r\rangle \propto t^{1/5}$, which is expected for the case when bubbles are considered to be in equilibrium.

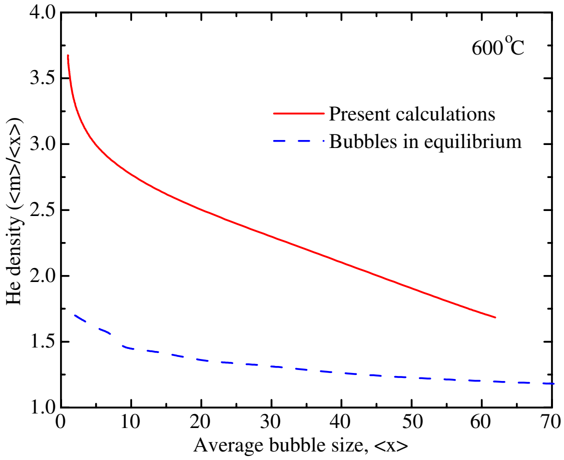

Fig. 5. Average density of He in bubbles as a function of average bubble size calculated for the case of annealing at 600 °C. Note that the same size dependence for equilibrium bubbles is also presented.

One can conclude that the present calculations agree with the observations [30].

Note that the actual bubble size in this case is probably even smaller than that calculated if we take into account that the mobility of over-pressurized bubbles has to be less than that described by Eq. (10). Indeed, it has been shown (see e.g. [9,22]) that high He pressure in bubbles suppresses vacancy surface diffusion and consequently bubble mobility. From Fig. 5 it is clearly seen that the strongest suppression of bubble mobility would take place during the earlier stages of annealing when the He density in bubbles is very high. Thus, the onset of bubble evolution is probably delayed and consequently their size will be smaller than that found in our calculations.

4.3. Impact of equation of state

Bubble stability with respect to vacancy emission is determined by the corresponding binding energy, which depends on the bubble gas pressure that is calculated via EOS. Taking the non-ideal EOS in a form $p(x,m) = nk_BT{*}Z(m/x,T)$, the vacancy binding energy with a bubble containing x vacancies and m He atoms may be presented as follows:

$$E_v^b(x,m) = E_v^f - \frac{\alpha}{x^{1/3}} + \left(\frac{m}{x}\right)Z\left(\frac{m}{x},T\right)k_BT, \qquad (12)$$

where $n = m/x\Omega$ is the bubble gas density, k_B and T are the Boltzmann constant and absolute temperature, respectively, $Z(m/x,T) \geqslant 1$ is the so-called compressibility factor, E_v^f is the vacancy formation energy, and $\alpha = 2\gamma(4\pi\Omega^2/3)^{1/3}$. As can be seen from Eq. (12) $E_v^b(x,m)$ decreases the compressibility factor decreases. In the case when the ideal EOS is applied the compressibility factor reaches a minimum value, $Z(m/x,T) = 1$, and consequently $E_v^b(x,m)$ also reaches a minimum value. Because the ideal EOS has a very simple form it has been often used in the past to describe bubble evolution in both analytically and numerically models. For example, the simplest description of He bubble evolution may be obtained assuming that during annealing (a) all bubbles are in mechanical equilibrium and (b) all bubbles are characterized by a mean radius (delta function approach). In this case, the density and mean radius of bubbles are given by (see e.g. [38])

$$\begin{aligned} r &= 1.48 * \left(\frac{Mk_{\mathrm{B}}T\Omega^{4/3}}{2\gamma}\right)^{1/5}(D_{\mathrm{S}}t)^{1/5}, \\ N &= 0.256 * \left(\frac{3Mk_{\mathrm{B}}T}{8\pi\gamma\Omega^{8/9}}\right)^{3/5}(D_{\mathrm{S}}t)^{-2/5}, \end{aligned} \qquad (13)$$

where M is the total number of He atoms in a unit volume. Eq. (13) have been often used for comparisons with experimental observations (see e.g. [36]), although the validity of the model has never been verified. Such verification can be easily done by repeating the calculations while employing the ideal EOS. Comparison of the calculated results obtained with the ideal EOS with those obtained with the non-ideal EOS and given by Eq. (13) reveal the impact of EOS on the predicted bubble evolution and also verify the validity of Eq. (13). Note that Eq. (13) are slightly different than those given in [38] due to the reduction of the rate in Eq. (13.252) in [38] by a factor of 2 since removal of two bubbles in a coalescence event forms another bubble firstly noted in [39].

Such a comparison is presented in Figs. 6 where the density and mean size of bubbles are plotted as a function of the annealing time calculated in three different ways at 800 °C. The solid and short dashed curves on the plots represent the calculated results obtained by numerical integration of Eqs. (6)–(8) with non-ideal and ideal EOS, respectively, whereas the long dashed lines are calculated using Eq. (13). As can be seen from Fig. 6(a), the bubble density calculated with the non-ideal EOS is always higher than that calculated with the ideal EOS except for the initial stage. Moreover, the difference increases with time because in the case of the ideal EOS the density decreases more rapid with time. However, at large enough time (>10^3 s), when the bubble density calculated for the ideal EOS reaches a value close to that given by Eq. (13), the time dependence is changed to nearly of $\sim t^{-2/5}$, i.e. very close to that given by Eq. (13). Surprisingly, in the non-ideal ES case, the time dependence follows a law which is also very close $\sim t^{-2/5}$ after about 10 annealing seconds even though the bubble density is higher than that given by Eq. (13).

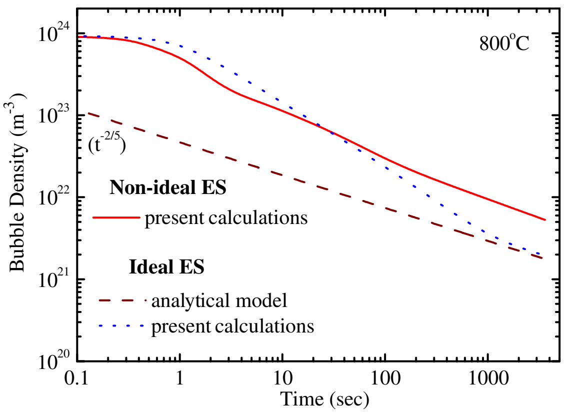

Fig. 6(a). Time dependence of the bubble number density at 800 °C during annealing for 1 h calculated using the non-ideal and ideal equations of state, and Eq. (13).

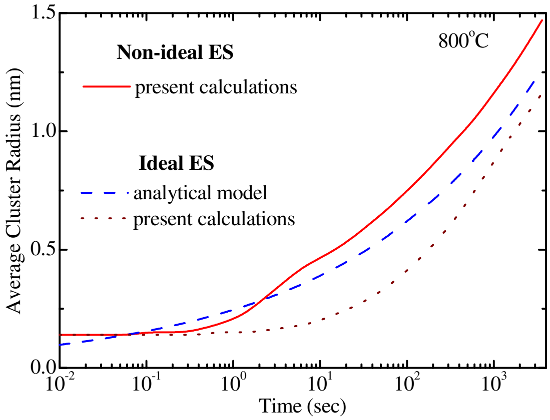

Fig. 6(b). Time dependence of the bubble size at 800 °C during annealing for 1 h calculated using the non-ideal and ideal equations of state.

As can be seen from Fig. 6(b), the mean size calculated in the case of the non-ideal ES is also higher than that calculated in the case of the ideal ES. However the difference is not as large as in the case of the bubble density. Similar to that found for the density the time dependence of the mean size in the case of non-ideal ES is also close to that for the ideal ES at large enough annealing times. Moreover the time dependence is close to that given by Eq. (13). Thus, although the total volume of bubbles calculated in the case of the non-ideal ES is found to be essentially larger than that calculated in the case of the ideal ES, the time dependences of both density and mean size of bubbles in both cases follow approximately the same law at large enough annealing times. Moreover, this time dependence is very close to that given by Eq. (13). Thus, one may conclude that the main effect caused by the non-ideal ES relative to the ideal ES is an increase in the absolute values of the density and size of bubbles whereas their evolution in time is very similar in both cases.

The validity of Eqs. (13) can be verified by comparison of the short dashed curves and long dashed curves in Figs. 6. It can be seen that at the intermediate annealing times Eq. (13) underestimates the density and overestimates the mean size of bubbles compared to that obtained by the numerical integration. However the effects decrease with increasing annealing time and finally the difference between the numerical results and those described by (13) becomes very small. Thus, one may conclude that bubble evolution described by Eq. (13) is quite reasonable at high enough annealing times. Note that this conclusion is valid in the case when the mean bubble size is large enough to apply the ideal ES.

5. Conclusions

A new grouping method developed to obtain an approximate solution of two-dimensional ME describing the evolution of point defect clusters proposed in [28,29] has been applied to calculate He bubble evolution in a stainless steel irradiated with alpha particles near room temperature and annealed in the temperature range of 600–900 °C. For the first time the bubble evolution during annealing driven by Brownian motion and coalescence has been calculated without the assumption that bubbles remain in mechanical equilibrium during the process. The calculated results shown:

1. Brownian motion and coalescence of bubbles provide a reasonable mechanism for explaining bubble evolution during annealing in the whole temperature range. The surface diffusion coefficient obtained from the calculations agrees well with that reported for a similar stainless steel at similar temperatures [36].
2. Average size and number density of bubbles after annealing for 1 h calculated in the temperature range of 700–900 °C agree well with those measured in [30]. It is found that the 2-D bubble size distribution calculated in this temperature range covers a quite narrow area in the x, m-phase space located along the equilibrium trajectory ($p = 2\gamma/r$). One may conclude that the assumption that bubbles remain in mechanical equilibrium during annealing used in the earlier models is quite realistic at high enough temperatures.
3. Bubble coarsening occurs also at 600 °C but the average bubble size remains too small during the annealing to be detected by TEM agrees well with the observations. Slow bubble growth in this case is related not only to a decrease in cluster mobility but also due to a lack of freely migrating vacancies since the annealing time of 1 h is not enough to build up the thermal equilibrium vacancy concentration. As a result, bubbles remain over-pressurized during the annealing. Because of this pressurization, the mobility of bubbles at this temperature is probably overestimated in our calculations, i.e. the bubble size has to be even smaller, since high gas pressure should suppress surface diffusion and consequently bubble coalescence.
4. Bubble evolution is quite sensitive to the He equation of state used for the calculations in the bubble size range of several nanometers. When a non-ideal EOS is used to calculate bubble evolution, both the density and size of bubbles are larger than that calculated with the ideal gas EOS. It is found also that a simple model for bubble evolution based on a mean size approach of type given by Eq. (13) may give a quite realistic description of the process at long enough annealing times and high temperatures.

References

[1] K. Russell, Acta Metall. 19 (1971) 753;
K. Russell, Acta Metall. 26 (1978) 1616.
[2] S.I. Maydet, K. Russell, J. Nucl. Mater. 82 (1979) 271.
[3] J.L. Katz, H. Wiedersich, J. Nucl. Mater. 46 (1973) 41.
[4] B.N. Singh, A.J.E. Foreman, in: R.S. Nelson (Ed.), The Physics of Irradiation Produced Voids, HMSO, London, 1975, p. 205.
[5] H. Wiedersich, J.J. Barton, J.L. Katz, J. Nucl. Mater. 51 (1974) 287.
[6] H. Trinkaus, J. Nucl. Mater. 118 (1983) 39.

[7] A.J.E. Foreman, B.N. Singh, J. Nucl. Mater. 141–143 (1986) 672.

[8] H. Trinkaus, B.N. Singh, A.J.E. Foreman, J. Nucl. Mater. 174 (1990) 80.

[9] B.N. Singh, H. Trinkaus, J. Nucl. Mater. 186 (1992) 153.

[10] B.N. Singh, A.J.E. Foreman, J. Nucl. Mater. 122&123 (1984) 537.

[11] N.M. Ghoniem, H. Gurol, Radiat. Eff. 55 (1981) 209.

[12] S. Sharafat, N.M. Ghoniem, J. Nucl. Mater. 122&123 (1984) 531.

[13] N.M. Ghoniem, J. Nucl. Mater. 174 (1990) 168.

[14] M.V. Speight, J. Nucl. Mater. 12 (1964) 216.

[15] E.E. Gruber, J. Appl. Phys. 38 (1967) 243.

[16] E.E. Gruber, in: J.W. Corbet, L.C. Iannielo (Eds.), Radiation-Induced Voids in Metals, USAEC-Conf. 71061, Albany, 1972, p. 663.

[17] G.W. Greenwood, M.V. Speight, J. Nucl. Mater. 10 (1963) 140.

[18] P.J. Goodhew, S.K. Tyler, in: Proc. of the R. Soc. of London A377 (1988) 151.

[19] E.Y. Mikhlin, Phys. Status Solidi A 56 (1975) 331.

[20] D. Preininger, D. Kaletta, J. Nucl. Mater. 117 (1983) 239; D. Preininger, D. Kaletta, J. Nucl. Mater. 122&123 (1984) 520.

[21] M. Fell, S.M. Murphy, J. Nucl. Mater. 172 (1990) 1.

[22] V.F. Chkuaseli, J. Nucl. Mater. 188 (1992) 258.

[23] V. Zell, H. Trinkaus, H. Schroeder, J. Nucl. Mater. 212–215 (1994) 320.

[24] J.H. Evans, Nucl. Instrum. Meth. Phys. Res. B 196 (2002) 125.

[25] J.H. Evans, J. Nucl. Mater. 334 (2004) 40.

[26] M. Kiritani, J. Phys. Soc. Jpn. 35 (1973) 95.

[27] S.I. Golubov, A.M. Ovcharenko, A.V. Barashev, B.N. Singh, Philos. Mag. Series A 81 (3) (2001) 643.

[28] S.I. Golubov, R.E. Stoller, S.J. Zinkle, Fusion Materials Semiannual Progress Report, 2002, DOE/ER-0313/33, US Department of Energy, 155.

[29] S.I. Golubov, R.E. Stoller, S.J. Zinkle, Fusion Materials Semiannual Progress Report, 2003, DOE/ER-0313/35, US Department of Energy, 214.

[30] R.E. Stoller, G.R. Odette, J. Nucl. Mater. 154 (1988) 286.

[31] S. Chandrasekhar, Rev. Mod. Phys. 15 (1943) 1.

[32] F.A. Nichols, J. Nucl. Mater. 30 (1969) 143.

[33] R. Manzke, W. Jäger, H. Trinkaus, G. Crecelius, R. Zeller, Solid State Commun. 44 (4) (1982) 481.

[34] H. Trinkaus, Radiat. Eff. 78 (1983) 189.

[35] D.D. McCracken, W.S. Dorn, Numerical Methods and Fortran Programming, John Wiley, 1965 (2nd printing).

[36] F.A. Smidt Jr., A.G. Pieper, Properties of Reactor Structural Alloys after Neutron or Particle Irradiation, ASTM STP 570, American Society for testing and Materials, 1975, p. 352.

[37] R.E. Stoller, G.R. Odette, in: F.A. Garner, N.H. Packan, A.S. Kumar (Eds.), ASTM STP 955, ASTM, Philadelphia, 1987, p. 371, material parameters.

[38] Donald R. Olander, Fundamental Aspects of Nuclear Reactor Fuel Elements, TID-26711-P1, 1976, p. 243.

[39] R. Vassen, H. Trinkaus, P. Jung, Phys. Rev. B 44 (1991) 4206.